ACS OMEGA

http://pubs.acs.org/journal/acsodf

Article

Photothermal Reshaping of One-Dimensional Plasmonic Polymers: From Colloidal Dispersion to Living Cells

Dorothy Bardhan, Hirak Chatterjee, Debarun Sen, Mahuya Sengupta, and Sujit Kumar Ghosh*

Cite This: *ACS Omega* 2022, 7, 11501−11509

Read Online

ACCESS | Metrics & More | Article Recommendations | Supporting Information

ABSTRACT: Cellular internalization of plasmonic metal nanostructured materials has recently become a requisite for biomedical engineering of several intracellular processes that could foster an extensive paradigm to perform desired functions in the living cells. While numerous anisotropic metal nanostructures can be employed to pursue the specific functions, their incorporation becomes restricted due to morphological specificity to be engulfed in the cells. Due to recent advent in the self-assembly strategies, individual gold nanospheres could be interdigitated to one-dimensional plasmonic polymers and undergo subsequent laser-induced photothermal reshaping to rod-like nanostructures. The salient feature of biological significance is merely the variation of particle size within the polymers that engenders a dramatic impact on the radiative and nonradiative properties expressed in the scale of Faraday number (F_a) and Joule number (J_0), respectively, as a function of the aspect ratio (α) of the nanorods. The effect on the nonradiative properties augments designing of nanoscale thermometry essential for photothermal applications in living cells. The conception of the colloidal dispersion has been extended to the cellular environment in a mice model; the selective accumulation of the nanostructures in the cells could provide an invading relationship between plasmonic characteristics, temperature distribution, and the biological issues. The critical correlation between optical and thermal characteristics toward biomedical manipulation from both theoretical and experimental perspectives could augment a milestone toward the progress of modern medical sciences.

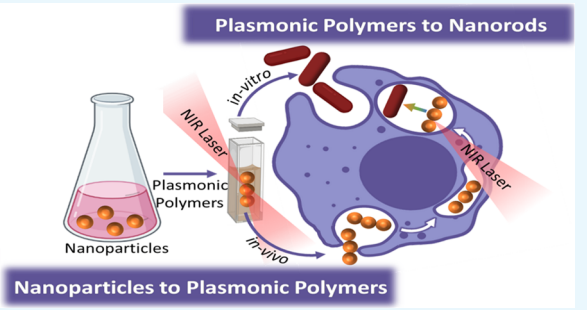

1. INTRODUCTION

The present era of precision nanomedicine is so proficiently popularized that it is anticipated to reach the global market of smart healthcare by 261 billion USD in 2023.[1] To overcome the challenges that lie ahead, one of the keys to success is the controlled and specific cellular administration of the nanostructures to design a landscape toward the novel biomedical applications.[2−4] Noble metals, at the nanoscale dimension, exhibit a strong photon-driven coherent oscillation of the surface conduction electrons under appropriate illumination coined as localized surface plasmon resonance (LSPR).[5] Metallic nanostructures show enhanced scattering and absorption of light in the UV−visible−NIR region of the electromagnetic spectrum. Owing to absorption cross sections with sizes up to several times the geometrical size, the absorbed light in metallic nanostructures is converted into thermal energy through several nonradiative relaxation processes other than heat dissipation.[6] The laser heating of the absorbing nanostructures has been found to be promising for the synthesis and fabrication of desired materials with spatiotemporal control and precision at the nanoscale to the macroscale, which has often been coined under the umbrella term laser synthesis and processing of colloids (LSPC).[7] Among different approaches that could be engendered for internalization of nanostructures inside the living cells, plasmonic heating of noble metal nanostructures can be employed as the energy-efficient avenue to cater varieties of isotropic and anisotropic nanostructures.[8] The application of plasmonic photothermal nanostructures has fostered enormous and extensive applications toward diverse frontiers of niche biomedical realms,[9−12] including drug delivery and release, biosensing, optical storage, selective killing of pathogenic bacteria, endosomal release of genes, photothermal destruction of malignant cells, and nonbiomedical applications,[13] such as nanocatalysis, chemical separation, nanofluidics, thermophotovoltaics, and so on. In addition, the observation of numerous thermoplasmonic attributes, *viz.*, photothermal chirality (differential circular absorption of chiral plasmonic nanostructures),[14] evolution of plasmonic nanobubbles (bubbles generated around the nanostructures due to plasmonic heating),[15] temperature-dependent anti-Stokes photolumines-

Received: February 28, 2022
Accepted: March 16, 2022
Published: March 25, 2022

cence emission,[16] and thermal contrast sufficient enough for imaging, has been the basis of photothermal microscopy.[17]

Prolific control of geometry and composition of the nanostructures governs their optimum biomedical applications.[18] Several anisotropic nanostructures, such as nanorods,[19] nanowires,[20] nanostars,[21] nanocages,[22] and nanoshells,[23] have often been employed to internalize inside the malignant cells through the enhanced permeation and retention (EPR) mechanism; however, because of their size heterogeneity and specific permissible dimensionality allowed, the intrinsic semipermeable characteristics of the membrane of healthy cells make them mostly reluctant to engulf these anisotropic nanostructures.[24] In the dilemma, living cells easily swallow spherical nanoparticles; therefore, one-dimensional assemblies of nanostructures interdigitated from isotropic spherical geometries could offer an ideal avenue for internalization inside healthy cells. The incorporation of such organized assemblies possesses several advantages. First, the plasmonic extinction band evolved as a result of polymeric nanostructures that impart spectral tunability into the biological tissue transparency windows that could be tuned to tailor specific biomedical application.[25] Second, the selective accumulation of one-dimensional assemblies of spherical nanostructures in a confined environment renders efficient heat generation in comparison with that of individual nanospheres.[26] Third, upon laser irradiation of the linearly organized nanostructures, the ensuing temperature change can be transmitted through multiple scales from the nanoparticle surface up to the bulk of the biological environment.[27] Finally, since the temperature becomes the key control parameter on a cellular-length scale in living organisms, the precise control of temperature through controlled interdigitation to polymeric nanostructures leads to the design of nanoscale thermometry that has remained as an outstanding challenge over the decades.[28] Therefore, the investigation of physical chemistry perspectives through spectroscopic techniques and theoretical models to characterize the thermoplasmonic characteristics is indispensable to augment the conception from the colloidal dispersion inside the living cells.[29]

In this article, we have demonstrated a thermoplasmonic footstep toward the *in vitro* photothermal reshaping of one-dimensional plasmonic polymers upon laser-induced melting in confined media like a cellular environment. Five different sets of plasmonic polymers obtained through interdigitation of size-selective constituent monomers have been internalized, and subsequent photothermal reshaping leads to the transformation to quasi-rod-like nanostructures with different aspect ratios. The spatial and temporal variations of temperature around the nanostructures have been calculated from both the theoretical and experimental perspectives. The discrete dipole approximation (DDA) technique has been employed to simulate the optical properties, and the finite element method (FEM) has been adopted to calculate the effective modes of the nanostructures. The electromagnetic field and temperature profiles have been scaled through the estimation of Faraday number (F_a) and Joule number (J_0) as a function of the aspect ratio (α) of the nanorods to devise the nanoscale thermometry. The conception of the colloidal dispersion has been extended to the cellular environment employing splenic macrophages in a mice model to design a landscape toward plausible biomedical engineering inside the living cells.

2. EXPERIMENTAL SECTION

2.1. Reagents and Instruments. All the reagents used were of analytical reagent grade. Hydrogen tetrachloroaurate ($HAuCl_4 \cdot 3H_2O$), silver nitrate ($AgNO_3$), cetyltrimethylammonium bromide (CTAB), L(+)-ascorbic acid, tannic acid, sodium borohydride ($NaBH_4$), sodium chloride (NaCl), 4′,6-diamidino-2-phenylindole dihydrochloride (DAPI), Histopaque-1077, Dulbecco's phosphate-buffered saline (DPBS), RPMI 1640 medium, 4-(2-hydroxyethyl)piperazine-1-ethanesulfonic acid (HEPES), and fetal bovine serum (FBS) were purchased from Sigma-Aldrich and were used as received. Annexin V-FITC conjugates (green) (Invitrogen) and ethanol (Qualigens Fine Chemicals) were purchased and used without further purification. Double-distilled water was used throughout the course of this investigation. For animal experiments, 6 to 7 week-old LACA male Swiss albino mice having a body weight of 20 ± 2 g were purchased from Pasteur Institute, Shillong, India (license no.: 34/DR/1966). The mice were accommodated in polycarbonate cages at 22 ± 2 °C temperature, 85% relative humidity, and 12 h light−dark cycles with standard food and water *ad libitum*. All treatments were carried out as per the guidelines of the Institutional Ethical Committee (IEC/AUS/2013−019, dated March 20, 2013).

The absorption spectra were measured in a PerkinElmer Lambda 750 UV−vis−NIR spectrophotometer by taking the sample in a 1 cm quartz cuvette. Transmission electron microscopy (TEM) was performed on a JEOL JEM-2100 microscope with a voltage of 200 kV. Samples were prepared by placing a drop of solution on a carbon-coated copper grid and dried overnight under vacuum. Laser heating was carried out with a continuous wave near-infrared diode laser (model: ML-III-785-1W; Changchun New Industries Optoelectronics Technology Co. Ltd., China) of 785 nm in wavelength and 1 W in output power by taking the sample in a 1 cm quartz cuvette. Dark-field imaging was carried out using an Olympus GX 51F inverted optical microscope by illuminating the sample with a halogen light source (U-LH100-3). The images of single nanostructures were placed at the entrance of an imaging spectrometer (SpectraPro 150, Acton Research), and the spectra were detected with a thermoelectrically cooled CCD camera (Prosilica GE680C). The infrared images were recorded on a Fluke Compact PTi120 pocket thermal camera, and the captured images were analyzed by Fluke Connect software. Fluorescence microscopy images of the cells stained with DAPI (excitation: 350 nm; detection: 470 nm) were recorded in a Nikon Eclipse TS100 fluorescence microscope and analyzed using ImageJ software packages. Different simulation techniques, *viz.*, finite element method (FEM),[30] were performed using the COMSOL Multiphysics software package, and the scattering coefficients were calculated using the discrete dipole approximation scattering (DDSCAT) code.[31] The optical constants of bulk gold provided by Johnson and Christy[32] were used in all the calculations. A hand-written Python code was used to compute equilibrium temperature profiles of the nanostructures.[33]

2.2. Synthesis of Size-Specific Gold Nanospheres. Monodispersed gold nanoparticles of varying size distributions were synthesized using Frens' citrate reduction method.[34] In this method, it is possible to control the size of the particles by varying the [Au(III)]/[citrate] ratio during the reduction step. A standard procedure for the preparation of set E is as follows.

https://doi.org/10.1021/acsomega.2c01094
ACS Omega 2022, 7, 11501−11509

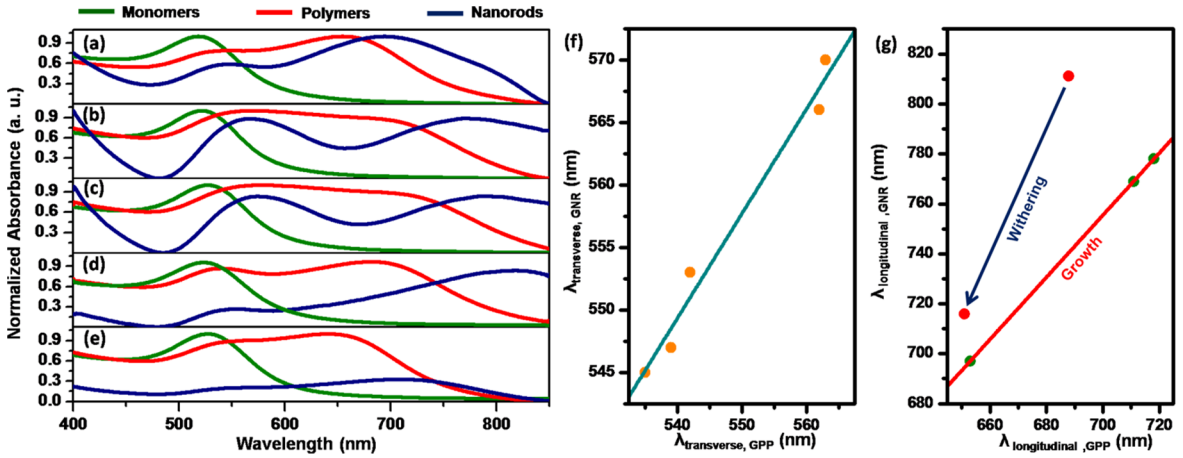

Figure 1. Extinction characteristics of the nanostructures: (a−e) extinction spectra of monomeric gold nanospheres and aggregation to one-dimensional plasmonic polymers upon laser-induced melting corresponding to particle sizes of 8, 13, 16, 20, and 32 nm, respectively. Panels (f) and (g) depict the linearity in transverse wavelength and nonlinearity in longitudinal wavelength during the photothermal transformation of GPPs to GNRs.

A 50 mL aqueous solution of $HAuCl_4.3H_2O$ (0.25 mM) was heated to boiling and 0.5 mL of trisodium citrate (1%) was quickly injected. In about 25 s, the boiling solution turned faintly blue (nucleation). After approximately 70 s, the blue color suddenly changed to brilliant red, indicating the formation of gold nanoparticles. A similar procedure was adopted for the other sets of particles. The particles formed by this method are spherical or nearly spherical with average diameters of *ca.* 8 ± 0.7, 13 ± 1.0, 16 ± 1.3, 20 ± 1.8, and 32 ± 4.0 nm designated as sets A−E, respectively.

2.3. Aggregation of Gold Nanospheres to Plasmonic Polymers. Using the citrate-stabilized gold nanoparticles as the building units, controlled aggregation among the negatively charged particles was induced by the addition of alcoholic solution of salt by following the protocol of Gu's group.[35] In a typical procedure, 2.0 mL aqueous dispersion of the as-prepared gold nanoparticles (0.25 mM) was precipitated through repeated washing with water and centrifugation at 10,000 rpm for 5 min, and finally, the volume was increased to 1.5 mL with distilled water. Then, a 15 μL aliquot of tannic acid (1%) and 0.5 mL ethanolic solution of NaCl (0.1 M) were added and the mixture was allowed to incubate for 30 min. The color of the dispersion immediately changed from reddish to bluish purple and finally to blue, indicating aggregation between the individual particles. A similar procedure was followed to induce aggregation for each set of gold nanoparticles.

2.4. Isolation of Splenic Macrophages. The isolation of splenic macrophages was carried out by following the experimental protocol demonstrated by Sengupta's group.[36] The spleens were isolated from adult male Swiss albino LACA (Laboratory Animal Centre A-strain) mice followed by immediate suspension in ice-cold Alsever's solution and saturation using frosted glass slides. A Pasteur pipette (sterilized) was used to obtain a single-cell suspension by aspiring through the pipette. The suspension (stored in sterile tubes) was kept in ice and the cell debris was allowed to settle. Histopaque-1077 (3.0 mL) was used to layer the supernatant followed by centrifugation at 1500 rpm for 15 min, and the entire process was repeated thrice. The leukocyte-enriched interface was collected and an ice-cold DPBS solution was used for washing. The whole process was repeated twice. The resuspension of cell pellet was carried out in RPMI-1640 having 20 mM HEPES (pH ∼7.2) and 5% FBS in the solution. The complete solution was allowed to adhere on the culture plate for 1 h at 37 °C in a 5% CO_2 incubator. The macrophages were adhered and collected by repeated aspiration with the Pasteur pipette, and the non-adhered macrophages were washed off. The whole-cell suspension was again washed off, finally resuspended in complete media (RPMI + FBS) at a density of 10^6 cells/mL, and stored in ice. A batch of more than 95% cells was found to be viable as determined by trypan blue staining.

2.5. Internalization of One-Dimensional Plasmonic Polymers in LACA Cells. Samples (500 mg) of the collected spleen tissues were treated with gold plasmonic polymers (GPPs) at the dose of 4 mg/kg b.w. The nanostructures were found to be adequately dispersed at the selected concentrations for at least 72 h, which was sufficient to perform cell culture experiments.

3. RESULTS AND DISCUSSION

In this experiment, monodispersed gold nanoparticles have been synthesized by varying the amount of citrate as the reducing and capping agent to achieve five different particle sizes, and subsequently, using these size-selective gold nanoparticles as the building blocks, ethanolic solution of sodium chloride in the presence of a trace amount of tannic acid has been added to synthesize GPPs of different sets. Details of the synthetic conditions for the preparation of monomeric gold nanoparticles, aggregation to one-dimensional polymeric nanostructures, and the distinctive LSPR characteristics are enunciated in Table S1.

The extinction characteristics of the nanostructures are illustrated in Figure 1. From panels (a)−(e), it is noted that while the monomers show a single characteristic plasmon band, with the increase in size of the gold nanoparticles, both wavelengths corresponding to the transverse and longitudinal polarizations for the GPPs are shifted. The GPPs upon treatment with an NIR laser result in the optothermal melting to gold rod-like nanostructures (GNRs). The plasmonic profiles signify two interesting phenomena. First, the plasmonic characteristics of GPPs and GNRs are similar for transverse polarization but change profoundly in the longitudinal

https://doi.org/10.1021/acsomega.2c01094
ACS Omega 2022, 7, 11501−11509

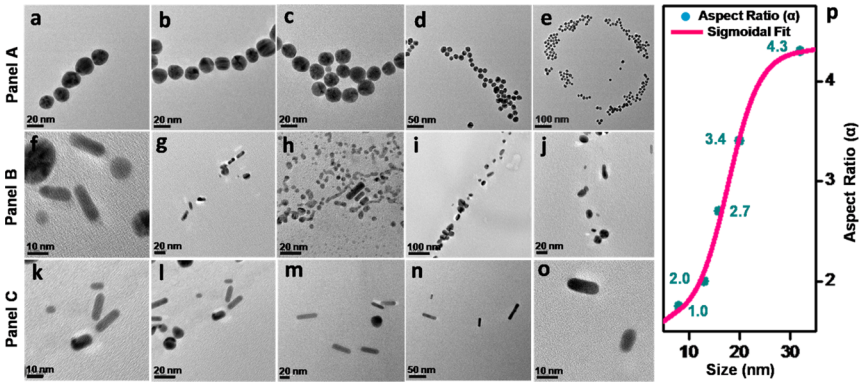

Figure 2. Morphological characteristics during photothermal reshaping: transmission electron micrographs of (a−e) one-dimensional aggregation of gold nanospheres, (f−j) laser-induced melting at the intermediate stage, and (k−o) thermally modified gold nanorods at the final stage corresponding to particle sizes of 8, 13, 16, 20, and 32 nm, respectively, and (p) plot of the aspect ratio of the photothermally transformed rod-like nanostructures as a function of corresponding monomer sizes obtained from transmission electron micrographs.

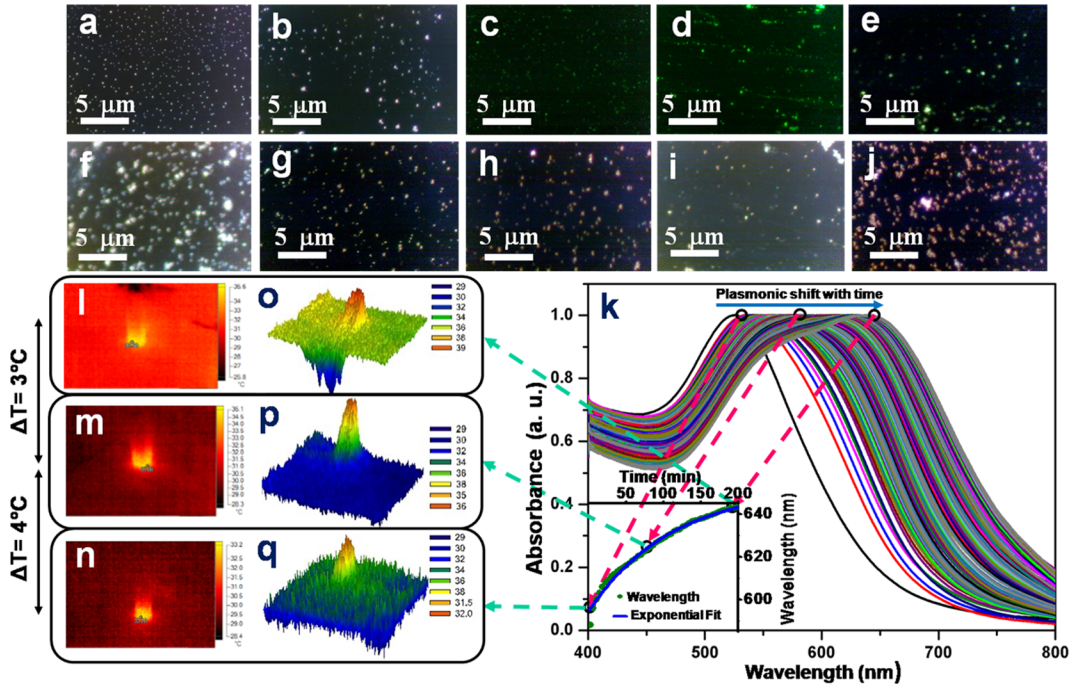

Figure 3. Spectral and thermal characteristics during photothermal reshaping: dark-field microscopy images showing (a−e) single polarization corresponding to monomers, (f−j) two different polarizations corresponding to one-dimensional aggregates for particle sizes of 8, 13, 16, 20, and 32 nm, respectively, and (k) gradual transformation of the localized surface plasmon resonance band upon laser-induced melting of one-dimensional aggregates of gold nanospheres (∼8 nm). The inset shows the variation of wavelength with time upon melting where the corresponding temperature distribution of (i) initial, (ii) anticipated intermediate, and (iii) final points is shown with images. (l−n) Corresponding thermal images and (o−q) processed surface plots.

polarization. While the mean difference in their transverse wavelengths varies within the 10 nm regime following linearity (panel f), after the formation of nanorods, the longitudinal bands red-shift to *ca.* 50 nm apart, indicating considerable extension in length without a major change in the diameter during the evolution of nanorods. Second, another interesting observation of physical significance is that above a critical diameter (*ca.* 16 nm) of the individual building blocks, instead of a higher relative red shift in the longitudinal peak, a sudden blue shift (panel g) implies withering in the average length of the evolved nanorods (marked by red data points). It therefore becomes evident that the chain length of GPPs decreases significantly above a threshold nanoparticle diameter, while the aspect ratio of GNRs remains unaffected. Beyond the critical diameter of 16 nm, this phenomenon could be explained considering the high surface energy of the small metallic particulates, leading to a reversible process of sintering and breakdown of melted GPPs toward the formation of GNRs.[37] Therefore, it becomes convenient to anticipate that with the increase in surface energy, the GPPs will contain more monomers sticking together to increase the chain length. With a further increase in monomer size, due to the weaker surface energy, the chain length of GPPs is reduced. However, during the electromagnetic melting, the GPPs are fused with either free monomers or another GPP to form GNRs of adequate aspect ratio.

Figure 2 displays the representative transmission electron micrographs of the different sets of GPPs (panel A),

https://doi.org/10.1021/acsomega.2c01094
ACS Omega 2022, 7, 11501−11509

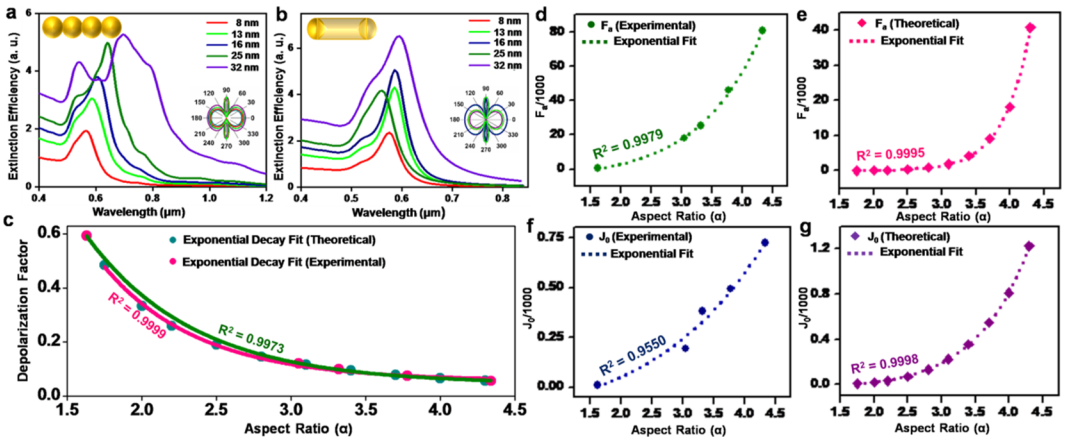

Figure 4. Photothermal properties upon laser-induced melting: (a) DDA-calculated extinction efficiency for (a) GPPs and (b) GNRs corresponding to different sizes of the monomeric building units. Insets show the polarization profiles calculated at the transverse and longitudinal peak points. Panel (c) shows comparative depolarization factors of nanorods from theoretical results and experimental outcomes as a function of their aspect ratio. A comparative account of the experimental and theoretical results for (d, e) Faraday number and (f, g) Joule number is presented with respect to the aspect ratio of the nanorods.

intermediate molten state (panel B), and transformation to the elongated rod-like nanostructures (panel C). To pursue the LSPC, GPPs were taken in a well-stoppered quartz cuvette (1 cm) and exposed to an NIR laser at an irradiance power of 0.90 mW. The sigmoidal fitting curve in profile (p) (R^2 = 0.9947) represents the trend of the aspect ratio of the elongated nanorods after LSPC with respect to the monomer size. The statistics of the aggregation to plasmonic polymers and subsequent photothermal transformation to nanorods are presented in Figure S1. It is observed that the number density decreases in both cases with increasing monomer size. Electromagnetic interaction between the monomers creates local hotspots at the junction. The electric field distribution patterns corresponding to transverse and longitudinal plasmon modes at the junction between the particles before and after melting of the polymers, which can act as a potential heat trapping region for the LSPC, are depicted in Figure S2. During the course of LSPC, the spectral characteristics have been determined through a dark-field spectrometer, which shows the kinetic change in the spectral profile of the GPPs to the ultimate reshaping of the nanorods as enunciated in Figure S3.

The photothermal transformation of GPPs to GNRs is elucidated in Figure 3. To achieve the conversion and document their concomitant change in optical signature, 10-fold dilution was carried out for the nanospheres and plasmonic polymer dispersions drop-casted on separate slides and thin films were prepared for the visualization through a green filter using a dark-field microscope. The evolution of transverse and longitudinal bands has been exhibited by observing the scattered beams, while the monomer having a single polarization (panels a−e) and GPPs exhibit both kinds (longitudinal and transverse) of polarizations (panels f−j) distinct from the captured five frames. The gradual evolution of the band at 653 nm is clearly observed from a clear single transverse band of monomers at *ca.* 535 nm (panel k). Upon the irradiance of a laser, the intensity of the transverse plasmon peak at 535 nm decreases gradually, implying the disappearance of plasmonic hotspots upon the fusion of monomers together forming the GNRs with the formation of a new band in the NIR region due to the evolution of longitudinal polarization. These morphological changes correspond to the thermal energy exchanged between the medium, nanostructures, and the laser beam, enumeration of which can furnish the thermodynamic characteristics for the LSPC of gold nanorods. To harness the intricate thermal exchange, where the infrared radiation absorbed is converted to an image, the thermal time stamps render a clear depiction of the temperature distribution profiles as displayed in Figure S4. The temperature gradient obtained from the thermal analyzer has been converted to the surface plots using a hand-written Python code as exhibited in Figure S5. To measure the rate of thermal exchange, we have judiciously selected three images. Throughout the entire set, we have chosen three points to measure the rate of thermal exchange: the first is set at 5 min after the beginning of the LSPC, the intermediate one is set at 100 min, and the terminal point corresponds to 200 min. From these limiting values of heat exchange and the corresponding nature of plasmon bands, we have explored the catastrophic change in their morphologies. A sharp plasmon band (monomeric gold nanospheres), eventual formation of a shoulder peak (for plasmonic polymer chains, GPPs), and finally, distinctive transverse and longitudinal peaks (for gold nanorods, GNRs) are clearly depicted in panel (k). The inset shows the exponential shift in the plasmon maximum with the temporal transformation in the geometry of the nanostructures. The dotted lines in conjugation with the three respective points for the corresponding states are acting as bridges between plasmonics and thermodynamics of the LSPC. Pairwise diagrams of the experimental thermal image along with the processed surface plot for thermal profiles at 200, 100, and 5 min after laser exposure are depicted through panels (l) and (o), (m) and (p), and (n) and (q), respectively. The salient feature of materials significance is that throughout the transformation, the system shows a stable thermal potential showing only a small rise of 3 °C during the successive steps from 5 to 100 min and 100 to 200 min of laser exposure, indicating a spontaneous stream of chemical potential for the shape transformation at the expense of electrical potential generated at the polymeric junctions.

The scattering characteristics for such transformations have been calculated based on discrete dipole approximation; we have assumed that the aspect ratio of the gold nanorods remains the same as the aspect ratio of the GPPs. A

https://doi.org/10.1021/acsomega.2c01094
ACS Omega 2022, 7, 11501−11509

comparative account of the theoretical calculations on the process of LSPC is shown cumulatively in Figure 4. Panel (a) represents the extinction efficiencies for plasmonic polymers comprised of five monomeric units with sizes of 8, 13, 16, 20, and 32 nm, respectively. The extinction efficiencies of the evolved nanorods are depicted in panel (b). Polarizations for both cases have been calculated at the transverse and longitudinal peak points and are shown in the insets of panels (a) and (b). The angular response of scattering with the orientation of the different sets of GPPs and the GNRs has been modeled through DDA calculations (Figure S6). The shape-selective scattering response of the GPPs and GNRs shows a steep growth in longitudinal peaks at *ca.* 570 and 600 nm, respectively, with the orientation toward 90° of the applied field for all five sets under consideration, while less intense multipolar peaks at ∼775 nm are shown by all the GPPs exclusively. More intricate studies on the polarization profiles (Figure S7) for all the modeled GPPs and the GNRs in their respective transverse and longitudinal peak wavelengths reveal that with the increase in length of the GPPs and GNRs, a gradual transition from dipolar mode to quadrupolar mode occurs for the transverse polarizations at higher angular distortions with respect to the scattering axis. The polarization patterns reveal symmetry for GNRs owing to equivalent forward- and backward-scattered waves for a complete rotation by 2π radians around the k_1 axis, but for GPPs, the pattern is asymmetrical; the same is also true for the quadrupolar plasmon modes. Although both GPPs and GNRs show symmetry in the polarization patterns at longitudinal wavelengths corresponding to smaller particle sizes, beyond the threshold diameter (*ca.* 16 nm), the polarization pattern for GPPs becomes twisted beyond $\pi/3$ radians. At a longer particle size regime (>32 nm), the polarization pattern at high angular distortion shows the emergence of asymmetric directionality, implying higher modes of electromagnetic coupling. Surprisingly, this effect is not shown by equidimensional GNRs, which remain pertinent toward their polarization pattern over the entire size regimes. This is due to the strong electromagnetic coupling at the NIR region; therefore, we have judiciously decided to excite the GPPs with wavelengths in the NIR region. From the extensive calculations of polarizations, we have calculated the depolarization factors of the gold nanorods of variable aspect ratios.

For ellipsoidal particles, Gans[38] proposed a relation between the depolarization factor (P_z) along the z-direction of polarization and the ellipticity (e) of both ends of prolate particles as

$$P_z = \frac{1-e^2}{e^2}\left[\frac{1}{2e}\left|\frac{1+e}{1-e}\right| - 1\right] = \frac{E_{0,z} - E_{i,z}}{\overrightarrow{L_z}} \quad (1)$$

where $E_{0,z}$ is the applied electric field, $E_{i,z}$ is the induced field, and L_z is the geometrical factor of depolarization along the z-direction. Replacing ellipticity with aspect ratio (α), the equation as converted into the form[21]

$$P_z = \frac{1}{\alpha^2-1}\left[\frac{\alpha}{2\sqrt{\alpha^2-1}}\ln\left|\frac{\alpha+\sqrt{\alpha^2-1}}{\alpha-\sqrt{\alpha^2-1}}\right| - 1\right] \quad (2)$$

For a generalized ellipsoidal geometry, the depolarization factor for the jth axis (L_j) can be presented in the form

$$\xi_j = \frac{1}{3}\frac{\varepsilon-\varepsilon_s}{\varepsilon_s + L_j(\varepsilon-\varepsilon_s)}, \text{ where } L_j = \frac{R_1R_2R_3}{2}\int_0^\infty \frac{du}{(u+R_j^2)\sqrt{(u+R_1^2)(u+R_2^2)(u+R_3^2)}} \quad (3)$$

where s and R_j are the surface area and half axis along the jth axis, respectively. In the above equation, R_1, R_2, and R_3 denote the radii of the ellipsoid along the principal axes, j = 1, 2, and 3, and L_j denotes the depolarization factor satisfying the relation $L_1 + L_2 + L_3 = 1$. The extinction spectra obtained through DDA calculation for the 10 different sets of gold nanorods with variable aspect ratios (assuming the variation in the length of the nanorods, keeping the width constant) are shown in Figure S8. Considering eq 1, the depolarization factors obtained from DDA calculations for the nanorods with different aspect ratios have been fitted with high precision and compared with the experimental depolarization factors obtained from dark-field spectroscopy. The comparative plot is shown in panel (c). Both the theoretical and experimental results indicate that the depolarization factors for nanorods decrease exponentially with the increase in the aspect ratio of the nanorods. With the increase in aspect ratio, the decrease in depolarization signifies extreme directionality toward the scattered wave, which again promotes significant applications of the nanorods out of strong directionality on the radiative electromagnetic effect as well as nonradiative photothermal processes.

To provide picturesque details about these effects, we have devised a model of the change in Faraday number (F_a) and Joule number (J_0) as a function of the aspect ratio of the GNRs, the parameters responsible for revealing the pervading effect of near-field coupling and photothermal efficiency, respectively. The electric field enhancement near the nanostructures is characterized by a dimensionless parameter, Faraday number (F_a), which is the squared ratio between the maximum electric near-field over space and the incoming electric field. The quantity is dependent on the dielectric constant of the medium as

$$F_a = \left|\frac{E}{E_0}\right|^2 = 9\left|\frac{\varepsilon}{\varepsilon+2\varepsilon_s}\right|^2 \quad (4)$$

This dimensionless parameter can effectively help compare among different materials, different wavelengths, and different environments at the electric field intensity, E_0, and refractive index, n_s. For spheroidal particles having the depolarization factor L_j, the Faraday number can be simplified into the form

$$F_a = \left[\frac{\varepsilon}{\varepsilon_s + L_j(\varepsilon-\varepsilon_s)}\right]^2 \quad (5)$$

For the linear assembly of plasmonic polymers, the depolarization factor is different from nanorods. This quantity signifies the electric field enhancement for both nanostructures and could be estimated from simultaneous theoretical (FEM studies in Figure S2) and experimental results. This quantity signifies the electric field enhancement yet is a poor indicator of the photothermal efficiency of the material. To estimate the photothermal efficiency of GNRs, we have estimated the Joule

https://doi.org/10.1021/acsomega.2c01094
ACS Omega 2022, 7, 11501−11509

number (J_0) for GNRs, bearing an aspect ratio at a fixed laser irradiance as

$$J_0 = \frac{e\varepsilon''}{n_s}|\xi - 1|^2 = 9\frac{e\varepsilon''}{n_s}\left|\frac{\varepsilon_s}{\varepsilon + 2\varepsilon_s}\right|^2 = \frac{\lambda_{ref}\sigma_{abs}}{2\pi V} \quad (6)$$

where σ_{abs} is the absorption cross section of the nanostructure, V denotes the nanoparticle volume, and λ_{ref} is set to 1240 nm. Now, to exploit the relationship for the anisotropic nanostructures, like nanorods having a small value of real dielectric constant (ε), we can use the approximated form of F_a as given by

$$F_a = \left[\frac{\varepsilon}{\varepsilon_s'' + L_j(\varepsilon - \varepsilon_s'')}\right]^2 \approx \frac{1}{L_j^2}\left|\frac{\varepsilon_s}{\varepsilon_s''}\right|^2 \quad (7)$$

where ε_s'' is the imaginary dielectric constant of the substrate. Based on this approximation, the Joule number becomes reduced to the form

$$J_0 = \frac{e\varepsilon''}{n_s}F_a \approx \frac{e}{L_j^2}\frac{n_s^3}{\varepsilon_s''} \quad (8)$$

The results obtained from the calculations from eqs 7 and 8 have been depicted in panels (d)−(g). The aspect ratio dependence of the Faraday number from both the experimental outcomes and theoretical calculations is illustrated in panels (d) and (e), respectively. Following a similar fashion, panels (f) and (g) represent the experimentally and theoretically calculated values of Joule number with respect to the aspect ratio of GNRs. All the calculations and experimental results illustrate an exponential increase in the values of Faraday number (F_a) and Joule number (J_0) for GNRs with an increase in aspect ratio, which ensures the increase in the photothermal efficacy with an increase in aspect ratio of the nanorods. Therefore, the derived protocol of LSPC from GPPs to GNRs can be exploited to specific photothermal applications.

Keeping these outcomes of the entire scientific experience in the backstage, we realized that it is feasible to convert GPPs to GNRs of controllable aspect ratio with a minimum change in medium temperature (*ca.* 3 °C) through photothermal reshaping in aqueous medium, which does bear a mere impact on the surroundings. The process is irreversible with measurable thermal signatures, which act as time stamps for the overall transformation. Therefore, the entire experience could open up multidimensional opportunities to apply the LSPC technique *in vitro* to uptake and transform the GPPs to GNRs in intracellular medium. The application has a unique importance because cells are rarely witnessed to uptake anisotropic nanostructures. The natural selectivity to cross the plasma membrane at the cell boundary imposes significant shape and size parameters toward the invading nanostructures, which cannot be altered. But the achievement toward the photothermal reshaping could be applied *in vitro* to reconfigure the shapes of penetrated nanostructures to transform to the desired shape as shown in Figure 5. In this regard, we have used splenic macrophages of Swiss albino mice and treated them with GPPs of constituent monomeric building units (~8 nm); the cellular dispersion was exposed to the laser as exhibited schematically in panel (A). The transmission electron micrographs captured before and after the exposure display the partial transformation of shape of uptaken spherical

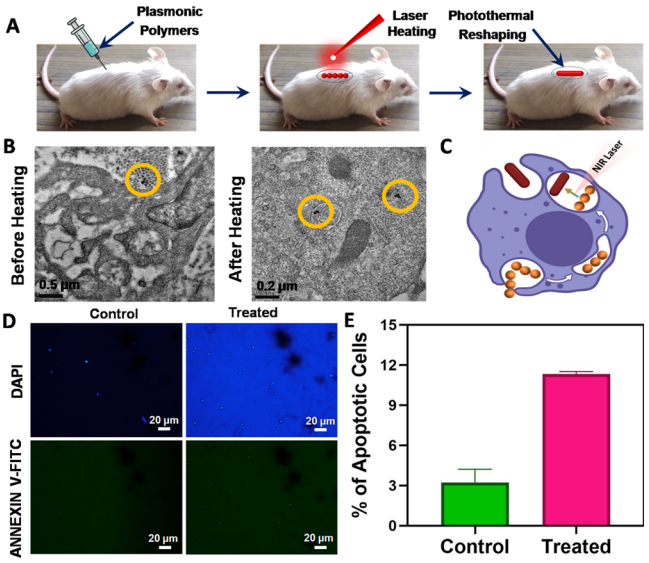

Figure 5. Photothermal reshaping of GPPs to GNRs inside the cellular environment: (A) schematic presentation showing accumulation of GPPs around the cell and subsequent photothermal reshaping to GNRs in a mice model, (B) transmission electron micrographs exhibiting photothermal reshaping of uptaken GPPs to GNRs inside the cells before and after laser irradiation, (C) schematic presentation of the plausible mechanism of the uptake and transformation of the GPPs to GNRs in intracellular medium, (D) fluorescence microscopy images of the cells using DAPI and annexin V-FITC fluorescence assays, and (E) statistical analysis (mean ± SEM) of the detection of apoptotic cells.

aggregates (panel B). A plausible mechanistic presentation of the uptake and transformation of the GPPs to GNRs in intracellular medium is shown in panel (C). Macrophages were then allowed to adhere to the media and the respective treatments were termed as untreated control and treated with GODPP (1.0 μM). After injecting the plasmonic polymers, the suspended media were aspirated off and washed with an ice-cold DPBS solution. A binding buffer (10 mM HEPES, 140 mM NaCl, and 2.5 mM $CaCl_2$) containing 10 mg/mL DAPI and annexin V-FITC according to manufacturers' instructions was used for resuspension of the cells and finally imaged under a fluorescence microscope. It is observed that the *in vitro* treatment of GODPP on LACA mice induces the apoptosis of the cancerous cells (panel D). The statistical analysis of the captured fluorescence images obtained by staining with DAPI and annexin V-FITC reveals the overall percentage of apoptotic cells (panel E); the cell death rate under treatment (>7%) is greater as compared to the control experiments (<5%). It can therefore be concluded that plasmonic polymers are effective in inducing apoptosis at relatively lower doses as evident from the fluorescence images developed with annexin V-FITC detected on apoptotic cells. Although the transformation is not well controlled, the protocol opens a new avenue toward *in vitro* LSPC, which will be investigated in detail in future studies.

4. CONCLUSIONS

In conclusion, we have demonstrated the cellular internalization of one-dimensional plasmonic polymers comprised of spherical gold nanoparticles as a viable avenue to incorporate anisotropic nanostructures for biomedical engineering inside the living cells. The assembly to quasi-linear polymeric fashion

https://doi.org/10.1021/acsomega.2c01094
ACS Omega 2022, 7, 11501−11509

from the monomeric gold nanoparticles and subsequent transformation to gold nanorods upon laser-induced melting could be explored to offer numerous possible opportunities toward biomedical applications including potential therapeutic modalities inside living cells. The variation of particle size impacts the evolution of gold nanorods of different aspect ratios that render the quantitative manipulation of temperature, implying nanoscale thermometry inside the living cells. The conception of the present methodology could be tailored to designing nanostructures with optimal thermoplasmonic properties for desired biomedical application that would pioneer overcoming some of the challenges in the present era of clinical translation of nanomedicines.

■ ASSOCIATED CONTENT

Supporting Information

The Supporting Information is available free of charge at https://pubs.acs.org/doi/10.1021/acsomega.2c01094.

Experimental details, statistical analysis, thermal measurements, calculation of electromagnetic fields, temperature distribution profiles, and scattering and polarization profiles (PDF)

■ AUTHOR INFORMATION

Corresponding Author

Sujit Kumar Ghosh − *Department of Chemistry, Assam University, Silchar 788011, India;* orcid.org/0000-0001-6657-7396; Phone: +91-3842-270848; Email: sujit.kumar.ghosh@aus.ac.in

Authors

Dorothy Bardhan − *Department of Chemistry, Assam University, Silchar 788011, India;* orcid.org/0000-0002-3769-8399

Hirak Chatterjee − *Department of Chemistry, Assam University, Silchar 788011, India;* orcid.org/0000-0002-2765-9900

Debarun Sen − *Department of Chemistry, Assam University, Silchar 788011, India;* orcid.org/0000-0001-7947-0643

Mahuya Sengupta − *Department of Biotechnology, Assam University, Silchar 788011, India;* orcid.org/0000-0001-9488-0368

Complete contact information is available at: https://pubs.acs.org/10.1021/acsomega.2c01094

Notes

The authors declare no competing financial interest.

■ ACKNOWLEDGMENTS

We gratefully acknowledge financial support from DST-SERB, New Delhi (project no.: EMR/2016/006842). We are thankful to Ramkrishna Pal and Nabanita Maity for helpful discussion on biological experiments.

■ REFERENCES

(1) Nanomedicine Market by Modality (Diagnostics and Treatment), Application (Drug Delivery, Diagnostic Imaging, Vaccines, Regenerative Medicine, Implants, and Others), and Indication (Clinical Oncology, Infectious Diseases, Clinical Cardiology, Orthopedics, Neurology, Urology, Ophthalmology, Immunology And Others): Global Opportunity Analysis and Industry Forecast, 2021−2030. https://www.alliedmarketresearch.com/nanomedicine-market.

(2) Giljohann, D. A.; Seferos, D. S.; Daniel, W. L.; Massich, M. D.; Patel, P. C.; Mirkin, C. A. Gold Nanoparticles for Biology and Medicine. *Angew. Chem., Int. Ed.* **2010**, *49*, 3280−3294.

(3) Ali, M. R. K.; Wu, Y.; El-Sayed, M. A. Gold-Nanoparticle-Assisted Plasmonic Photothermal Therapy Advances Toward Clinical Application. *J. Phys. Chem. C* **2019**, *123*, 15375−15393.

(4) Murphy, C. J.; Chang, H.-H.; Falagan-Lotsch, P.; Gole, M. T.; Hofmann, D. M.; Hoang, K. N. L.; McClain, S. M.; Meyer, S. M.; Turner, J. G.; Unnikrishnan, M.; Wu, M.; Zhang, X.; Zhang, Y. Virus-Sized Gold Nanorods: Plasmonic Particles for Biology. *Acc. Chem. Res.* **2019**, *52*, 2124−2135.

(5) Ghosh, S. K.; Pal, T. Interparticle Coupling Effect on the Surface Plasmon Resonance of Gold Nanoparticles: From Theory to Applications. *Chem. Rev.* **2007**, *107*, 4797−4862.

(6) Link, S.; El-Sayed, M. A. Shape and Size Dependence of Radiative, Non-Radiative and Photothermal Properties of Gold Nanocrystals. *Int. Rev. Phys. Chem.* **2000**, *19*, 409−453.

(7) Zhang, D.; Gökce, B.; Barcikowski, S. Laser Synthesis and Processing of Colloids: Fundamentals and Applications. *Chem. Rev.* **2017**, *117*, 3990−4103.

(8) Jauffred, L.; Samadi, A.; Klingberg, H.; Bendix, P. M.; Oddershede, L. B. Plasmonic Heating of Nanostructures. *Chem. Rev.* **2019**, *119*, 8087−8130.

(9) Baffou, G.; Cichos, F.; Quidant, R. Applications and Challenges of Thermoplasmonics. *Nat. Mater.* **2020**, *19*, 946−958.

(10) Jain, P. K.; Huang, X.; El-Sayed, I. H.; El-Sayed, M. A. Noble Metals on the Nanoscale: Optical and Photothermal Properties and Some Applications in Imaging, Sensing, Biology, and Medicine. *Acc. Chem. Res.* **2008**, *41*, 1578−1586.

(11) Jaque, D.; Martínez Maestro, L.; del Rosal, B.; Haro-Gonzalez, P.; Benayas, A.; Plaza, J. L.; Martín Rodríguez, E.; García Solé, J. Nanoparticles for Photothermal Therapies. *Nanoscale* **2014**, *6*, 9494−9530.

(12) Kim, M.; Lee, J.-H.; Nam, J.-M. Plasmonic Photothermal Nanoparticles for Biomedical Applications. *Adv. Sci.* **2019**, *6*, 1900471.

(13) Mateo, D.; Cerrillo, J. L.; Durini, S.; Gascon, J. Fundamentals and Applications of Photo-Thermal Catalysis. *Chem. Soc. Rev.* **2021**, *50*, 2173−2210.

(14) Rafiei Miandashti, A.; Khosravi Khorashad, L.; Kordesch, M. E.; Govorov, A. O.; Richardson, H. H. Experimental and Theoretical Observation of Photothermal Chirality in Gold Nanoparticle Helicoids. *ACS Nano* **2020**, *14*, 4188−4195.

(15) Moon, S.; Zhang, Q.; Xu, Z.; Huang, D.; Kim, S.; Schiffbauer, J.; Lee, E.; Luo, T. Plasmonic Nanobubbles − A Perspective. *J. Phys. Chem. C* **2021**, *125*, 25357−25368.

(16) Barella, M.; Violi, I. L.; Gargiulo, J.; Martinez, L. P.; Goschin, F.; Guglielmotti, V.; Pallarola, D.; Schlücker, S.; Pilo-Pais, M.; Acuna, G. P.; Maier, S. A.; Cortés, E.; Stefani, F. D. *In Situ* Photothermal Response of Single Gold Nanoparticles through Hyperspectral Imaging Anti-Stokes Thermometry. *ACS Nano* **2021**, *15*, 2458−2467.

(17) Gaiduk, A.; Ruijgrok, P. V.; Yorulmaz, M.; Orrit, M. Detection Limits in Photothermal Microscopy. *Chem. Sci.* **2010**, *1*, 343−350.

(18) Behzadi, S.; Serpooshan, V.; Tao, W.; Hamaly, M. A.; Alkawareek, M. Y.; Dreaden, E. C.; Brown, D.; Alkilany, A. M.; Farokhzad, O. C.; Mahmoudi, M. Cellular Uptake of Nanoparticles: Journey Inside the Cell. *Chem. Soc. Rev.* **2017**, *46*, 4218−4244.

(19) Huang, X.; Neretina, S.; El-Sayed, M. A. Gold Nanorods: From Synthesis and Properties to Biological and Biomedical Applications. *Adv. Mater.* **2009**, *21*, 4880−4910.

(20) Herzog, J. B.; Knight, M. W.; Natelson, D. Thermoplasmonics: Quantifying Plasmonic Heating in Single Nanowires. *Nano Lett.* **2014**, *14*, 499−503.

(21) Chatterjee, H.; Rahman, D. S.; Sengupta, M.; Ghosh, S. K. Gold Nanostars in Plasmonic Photothermal Therapy: The Role of Tip Heads in the Thermoplasmonic Landscape. *J. Phys. Chem. C* **2018**, *122*, 13082−13094.

(22) Skrabalak, S. E.; Chen, J.; Au, L.; Lu, X.; Li, X.; Xia, Y. Gold Nanocages for Biomedical Applications. *Adv. Mater.* **2007**, *19*, 3177−3184.
(23) Rastinehad, A. R.; Anastos, H.; Wajswol, E.; Winoker, J. S.; Sfakianos, J. P.; Doppalapudi, S. K.; Carrick, M. R.; Knauer, C. J.; Taouli, B.; Lewis, S. C.; Tewari, A. K.; Schwartz, J. A.; Canfield, S. E.; George, A. K.; West, J. L.; Halas, N. J. Gold Nanoshell-Localized Photothermal Ablation of Prostate Tumors in a Clinical Pilot Device Study. *Proc. Natl. Acad. Sci.* **2019**, *116*, 18590−18596.
(24) Moscatelli, A. Strolling on a Cell Membrane. *Nat. Nanotechnol.* **2021**, *16*, 1302.
(25) Slaughter, L. S.; Willingham, B. A.; Chang, W.-S.; Chester, M. H.; Ogden, N.; Link, S. Toward Plasmonic Polymers. *Nano Lett.* **2012**, *12*, 3967−3972.
(26) Xu, C.; Pu, K. Second Near-Infrared Photothermal Materials for Combinational Nanotheranostics. *Chem. Soc. Rev.* **2021**, *50*, 1111−1137.
(27) Wang, J.; Zhang, Y.; Jin, N.; Mao, C.; Yang, M. Protein-Induced Gold Nanoparticle Assembly for Improving the Photothermal Effect in Cancer Therapy. *ACS Appl. Mater. Interfaces* **2019**, *11*, 11136−11143.
(28) Choi, J.; Zhou, H.; Landig, R.; Wu, H.-Y.; Yu, X.; von Stetinae, S. E.; Kucsko, G.; Mango, S. E.; Needleman, D. J.; Samuel, A. D. T.; Maurer, P. C.; Park, H.; Lukin, M. D. Probing and Manipulating Embryogenesis via Nanoscale Thermometry and Temperature Control. *Proc. Natl. Acad. Sci.* **2020**, *117*, 14636−14641.
(29) Hooshmand, N.; Thoutam, A.; Anikovskiy, M.; Labouta, H. I.; El-Sayed, M. A. Localized Surface Plasmon Resonance as a Tool to Study Protein Corona Formation on Nanoparticles. *J. Phys. Chem. C* **2021**, *125*, 24765−24776.
(30) Yee, K. Numerical Solution of Initial Boundary Value Problems involving Maxwell's Equations in Isotropic Media. *IEEE Trans. Antennas Propag.* **1966**, *14*, 302−307.
(31) Draine, B. T.; Flatau, P. J. Discrete-Dipole Approximation for Scattering Calculations. *J. Opt. Soc. Am. A* **1994**, *11*, 1491−1499.
(32) Johnson, P. B.; Christy, R. W. Optical Constants of the Noble Metals. *Phys. Rev. B* **1972**, *6*, 4370−4379.
(33) Phython. http://www.python.org.
(34) Frens, G. Controlled Nucleation for the Regulation of the Particle Size in Monodisperse Gold Suspensions. *Nature* **1973**, *241*, 20−22.
(35) Liao, J.; Zhang, Y.; Yu, W.; Xu, L.; Ge, C.; Liu, J.; Gu, N. Linear Aggregation of Gold Nanoparticles in Ethanol. *Colloids Surf., A* **2003**, *223*, 177−183.
(36) Chakraborty, B.; Pal, R.; Ali, M.; Singh, L. M.; Rahman, D. S.; Ghosh, S. K.; Sengupta, M. Immunomodulatory Properties of Silver Nanoparticles Contribute to Anticancer Strategy for Murine Fibrosarcoma. *Cell. Mol. Immunol.* **2016**, *13*, 191−205.
(37) Sau, T. K.; Pal, A.; Pal, T. Size Regime Dependent Catalysis by Gold Nanoparticles for the Reduction of Eosin. *J. Phys. Chem. B* **2001**, *105*, 9266−9272.
(38) Gans, R. Über die Form Ultramikroskopischer Goldteilchen. *Ann. Phys.* **1912**, *342*, 881−900.

https://doi.org/10.1021/acsomega.2c01094
ACS Omega 2022, 7, 11501−11509